The Astrophysical Journal Letters, 896:L22 (5pp), 2020 June 20 https://doi.org/10.3847/2041-8213/ab9530

Irradiated Ocean Planets Bridge Super-Earth and Sub-Neptune Populations

Olivier Mousis[1], Magali Deleuil[1], Artyom Aguichine[1], Emmanuel Marcq[2], Joseph Naar[1,2], Lorena Acuña Aguirre[1], Bastien Brugger[3], and Thomas Gonçalves[1]
[1] Aix Marseille Univ, CNRS, CNES, LAM, Marseille, France; olivier.mousis@lam.fr
[2] LATMOS/CNRS/Sorbonne Université/UVSQ, 11 boulevard d'Alembert, Guyancourt, F-78280, France
[3] Department of Astronomy, Cornell University, Ithaca, NY 14853, USA
Received 2020 March 27; revised 2020 May 19; accepted 2020 May 20; published 2020 June 15

Abstract

Small planets (∼1–3.9 $R_\oplus$) constitute more than half of the inventory of the 4000-plus exoplanets discovered so far. Smaller planets are sufficiently dense to be rocky, but those with radii larger than ∼1.6 $R_\oplus$ are thought to display in many cases hydrogen/helium gaseous envelopes up to ∼30% of the planetary mass. These low-mass planets are highly irradiated and the question of their origin, evolution, and possible links remains open. Here we show that close-in ocean planets affected by the greenhouse effect display hydrospheres in supercritical state, which generate inflated atmospheres without invoking the presence of large hydrogen/helium gaseous envelopes. We present a new set of mass–radius relationships for ocean planets with different compositions and different equilibrium temperatures, which are found to be well adapted to low-density sub-Neptune planets. Our model suggests that super-Earths and water-rich sub-Neptunes could belong to the same family of planets, i.e., hydrogen/helium-free planets, with differences between their interiors simply resulting from the variation in the water content.

Unified Astronomy Thesaurus concepts: Exoplanets (498); Hydrosphere (770); Planetary interior (1248); Planetary theory (1258); Exoplanet astronomy (486); Exoplanet structure (495)

1. Introduction

With radii ranging between those of the Earth (1 $R_\oplus$) and Neptune (∼3.9 $R_\oplus$), small planets constitute more than half of the inventory of the 4000-plus exoplanets discovered so far.[4] Smaller planets are sufficiently dense to be rocky, but those with radii larger than ∼1.6 $R_\oplus$ are thought to display large amounts of volatiles, including in many cases hydrogen/helium gaseous envelopes up to ∼30% of the planetary mass (Lopez et al. 2012; Weiss & Marcy 2014; Rogers 2015). With orbital periods less than 100 days, these low-mass planets are highly irradiated and their origin, evolution, and possible links are still debated (Dorn et al. 2017; Venturini & Helled 2017; Jin & Mordasini 2018; Zeng et al. 2019).

The composition of the small planet population is often assessed by comparing their mass and radius measurements, when available, to theoretical mass/radius relationships. While super-Earths appear compatible with more or less differentiated rocky planets, sub-Neptunes fall near nonphysical curves of planets composed of pure water, suggesting instead a solid core surrounded by a hydrogen/helium gaseous envelope up to ∼30% of the planetary mass (Lopez et al. 2012; Weiss & Marcy 2014; Rogers 2015; Dorn et al. 2017; Fulton et al. 2017; Venturini & Helled 2017; Fulton & Petigura 2018; Jin & Mordasini 2018; Zeng et al. 2019). However, even if the existence of sub-Neptunes with low metallicities (i.e., with hydrogen-rich atmospheres) is supported by spectroscopic observations (Benneke et al. 2019a), H_2O absorption bands have also been detected in the exo-Neptunes HAT-P-26b (MacDonald & Madhusudhan 2019) and K2-18b (Benneke et al. 2019b).

There is no clear consensus on how these small exoplanets populations might have formed. In situ formation faces a number of issues (Ogihara et al. 2015) and migration appears as the most likely scenario. In that case, planetary embryos or building blocks might have formed in the cold regions of the protoplanetary disk and migrated inward. As a result of their formation location, they should contain a significant fraction of water ice. This leads us to reconsider the possible existence of massive water-rich planets, as initially suggested by Léger et al. (2004). Water-rich worlds (Europa, Titan, Enceladus, Pluto, etc.) are ubiquitous in our solar system, and the building blocks of Neptune and Uranus are also supposed to be water-rich (Mousis et al. 2018). However none of the existing mass/radius relationships fully explores the physical properties of such ocean planets, i.e., planets displaying a significant fraction of liquid water (∼50 wt%), especially in the domain of high surface temperature. For instance, Zeng & Sasselov (2014) and Thomas & Madhusudhan (2016) pointed out the possible presence of supercritical water in ocean planets, but both were lacking in an atmospheric prescription. On the other hand, a recent investigation of mass–radius relationships for water-rich terrestrial planets (up to 5 wt% of water) endowed with water-dominated steam atmospheres suggests that such planets present radii larger than those of planets with water in liquid or solid phases (Turbet et al. 2020). However, this study needs further reassessment because the water layers of the most hydrated planets considered encompass pressure–temperature ranges corresponding to those of a supercritical fluid, which is not implemented in the used atmospheric model.

Here, to investigate the role of irradiation on ocean planets, we use a combination of two one-dimensional models, i.e., a fully differentiated planet interior model (Brugger et al. 2017) and a steam atmosphere model (Marcq 2012; Marcq et al. 2017) connected at a 1000 bar pressure, both using supercritical water equations of state (EOSs). We show that close-in ocean planets (Léger et al. 2004) affected by the greenhouse effect display hydrospheres in supercritical state, which generate

[4] https://exoplanetarchive.ipac.caltech.edu

inflated atmospheres without invoking the presence of large H/He gaseous envelopes. We derive a new set of mass–radius relationships for ocean planets with different compositions and different equilibrium temperatures, well adapted to low-density sub-Neptune planets. While it does not preclude the existence of other hydrogen–helium-rich sub-Neptunes, our model suggests that super-Earths and water-rich sub-Neptunes could belong to the same family of planets. The differences between their interiors could simply result from the variation of the water content in those planets.

2. Model

2.1. Interior Model

We use the internal model of the solid planet developed by Brugger et al. (2017). It takes as inputs the planetary mass and chemical composition (Mg/Si, Fe/Si mole ratios and water mass fraction), and computes the resulting radius and internal structure of the planet (Brugger et al. 2017). The internal structure computes the pressure $P(r)$, the temperature $T(r)$, the gravity acceleration $g(r)$, and the density $\rho(r)$ as a function of radius. These quantities are integrated following an iterative scheme until convergence is reached. Along the radius r of the planet, the pressure $P(r)$ is calculated via different EOSs, which are chosen depending on the material that composes the considered layer. The different layers include the core, the lower and upper mantles, the high pressure ice, and a liquid hydrosphere (Brugger et al. 2017). To account for the effects of irradiation, as expected for the close-in population, a water phase in supercritical state has been added to the hydrosphere. For a given density and temperature, the supercritical layer pressure is calculated via an EOS obtained from data generated by molecular level computer simulations that consider simple point-charge potential models to which average polarization corrections have been added (Duan & Zhang 2006, hereafter DZ06). This EOS is written as

$$Z = \frac{PV}{RT} = 1 + \frac{BV_c}{V} + \frac{CV_c^2}{V^2} + \frac{DV_c^4}{V^4} + \frac{EV_c^5}{V^5} + \frac{FV_c^2}{V^2} \times \left(\beta + \frac{\gamma V_c^2}{V^2}\right) \exp\left(-\frac{\gamma V_c^2}{V^2}\right), \quad (1)$$

where $R = 83.14467$ cm^3 bar/(K mol) is the universal gas constant. Parameters B, C, D, E, and F in Equation (1) are calculated via the following equations:

$$B = a_1 + \frac{a_2}{T_r^2} + \frac{a_3}{T_r^3}, \quad (2)$$

$$C = a_4 + \frac{a_5}{T_r^2} + \frac{a_6}{T_r^3}, \quad (3)$$

$$D = a_7 + \frac{a_8}{T_r^2} + \frac{a_9}{T_r^3}, \quad (4)$$

$$E = a_{10} + \frac{a_{11}}{T_r^2} + \frac{a_{12}}{T_r^3}, \quad (5)$$

$$F = \frac{\alpha}{T_r^3}, \quad (6)$$

$$T_r = \frac{T}{T_c}, \quad (7)$$

Table 1
EoS Parameters

Parameter	Value
a_1	$4.68071541 \times 10^{-02}$
a_2	$-2.81275941 \times 10^{-01}$
a_3	$-2.43926365 \times 10^{-01}$
a_4	$1.10016958 \times 10^{-02}$
a_5	$-3.86603525 \times 10^{-02}$
a_6	$9.30095461 \times 10^{-02}$
a_7	$-1.15747171 \times 10^{-05}$
a_8	$4.19873848 \times 10^{-04}$
a_9	$-5.82739501 \times 10^{-04}$
a_{10}	$1.00936000 \times 10^{-06}$
a_{11}	$-1.01713593 \times 10^{-05}$
a_{12}	$1.63934213 \times 10^{-05}$
α	$-4.49505919 \times 10^{-02}$
β	$-3.15028174 \times 10^{-01}$
γ	$1.25000000 \times 10^{-02}$

$$F = \frac{RT_c}{P_c}, \quad (8)$$

where T_c and P_c are the critical temperature and critical pressure, respectively. Here, $T_c = 647.25$ K, and $P_c = 221.19$ cm^3/mol. Parameters a_1–a_{12}, α, β, and γ valid in the 0.2–10 GPa range are summarized in Table 1. We refer the reader to the study of Duan & Zhang (2006) for details.

The resulting EOS (DZ06) agrees within a $\pm 0.6\%$ deviation with the well-known IAPWS95 formulation (Wagner & Pruß 2002), which provides an accurate EOS based on experimental data within the ~0–1.0 GPa pressure range. At higher pressure, the DZ06 EOS has been shown to compute the pressure within a $\pm 1.3\%$ deviation up to 10.0 GPa. Above, comparisons with simulated data (Duan et al. 1996; Duan & Zhang 2006) show it remains within a $\pm 5.0\%$ deviation up to 35 GPa.

The adiabatic temperature profile within the supercritical layer depends on the Grüneisen parameter, which has a strong dependence on both density and temperature. In the supercritical layer, this parameter is derived from a bilinear interpolation of a grid of data available in the python library for the International Association for the Properties of Water and Steam (IAPWS) standard calculation of water and steam properties.[5] This grid gives a range of Grüneisen parameters for temperatures up to 10^4 K and supercritical water densities up to 2500 kg m^{-3}, corresponding to pressures up to ~150 GPa, a value exceeding the one at the center of a 20 $M_\oplus$ planet fully made of water. When deriving this grid, the IAPWS team focused on the behavior of the extrapolation of the analytical formulation, and ensured it remains physically correct in domains of high pressure/temperature, which are relevant to exoplanetary interiors. The Grüneisen parameter's profile is then expected to have a correct physical behavior, albeit with increasing uncertainties when going deeper in the planet. However, we find this to be of secondary importance regarding planetary radius as the Grüneisen parameter is basically a proxy of thermal expansivity along pressure variations, which rapidly becomes of second order when pressure increases.

[5] https://pypi.org/project/iapws/#description

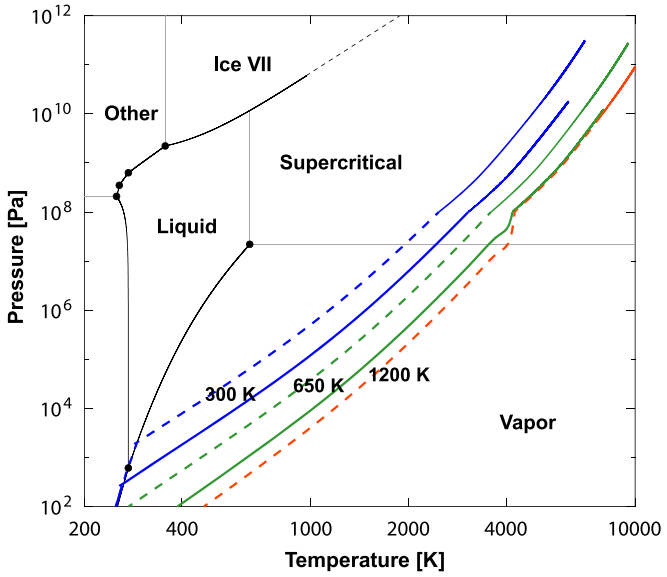

Figure 1. Pressure and temperature profiles of hydrospheres of 1 and 15 $M_\oplus$ supercritical ocean planets fully constituted of water with equilibrium temperatures of 300, 650, and 1200 K superimposed onto the water phase diagram. Colored solid and dashed curves correspond to 1 and 15 $M_\oplus$ planets, respectively. The black dashed line delimits a hypothetical transition between the supercritical phase and high pressure ice (see the text). Dashed lines change to solid lines when the interior model takes over from the atmosphere model. The 1 $M_\oplus$ case with an equilibrium temperature of 1200 K is removed because its atmosphere is hydrostatically unstable (see Figure 2).

2.2. Atmosphere Model

The atmosphere model (Marcq 2012; Marcq et al. 2017) takes over the hydrosphere at water column pressures lower than ∼1000 bar, where the H_2O envelope behaves more and more like a hot and dense steam atmosphere as the pressure drops. The used model is based on a $T(P)$ profile prescription (Kasting 1988) starting from the 1000 bar level (unsaturated since $T\,(1000\ \mathrm{bar}) > T_{\mathrm{critical}}$) upward, assuming a dry adiabat, and switching optionally to a moist adiabat (where $T(P) = T_{\mathrm{saturation}}(P)$) if/when saturation reaches unity. Once the temperature reaches the top temperature, here set to 200 K, an isothermal radiative mesosphere $T = T_{\mathrm{top}}$ is assumed up to the 0.1 Pa topmost level. Moreover, steam is not treated as an ideal gas, and the EOS is taken instead from the NBS/NRC steam tables (Haar et al. 1984). This enables a smooth transition of the $T(P)$ profile with the interior model at equilibrium temperatures of 300 and 650 K, at least. Altitudes are computed assuming hydrostatic equilibrium. Shortwave and thermal fluxes are then computed using 4-stream approximation. Gaseous (line and continuum) absorptions are computed using the k-correlated method. Rayleigh opacity is also included. $T\,(1000\ \mathrm{bar})$ is iteratively chosen so that the thermal flux at the top of the atmosphere is equal to σT_{eq}^4. We finally chose the radius/altitude of the 20 mbar level as the observable, transiting radius (Grimm et al. 2018).

3. Implications for the Mass–Radius Relationships

Figure 1 displays the pressure and temperature profiles (hereafter (P, T) profiles) of 1–15 $M_\oplus$ supercritical ocean planets fully constituted of water with equilibrium temperatures of 300, 650, and 1200 K, superimposed onto the water phase diagram. With the lack of rocky cores, these planets present unphysical interiors, but they have the merit to display hydrospheres over a large range of temperatures and pressures. The fluid–ice VII transition law is fitted from data between 3 and 60 GPa (Frank et al. 2004). The other phase-change laws are collected from a compilation of thermodynamic data (Wagner & Pruß, 2002), and from the website of the IAPWS.[6] The (P, T) profiles expand from the base of the hydrosphere (here the center of the planet) to the top of the H_2O-dominated atmosphere set to 0.1 Pa. Most of the hydrospheres remain in the supercritical regime and those of smallest planets are located well below ice VII, with a fluid–ice VII transition law valid up to 60 GPa (Frank et al. 2004) in the water phase diagram. Beyond this pressure range, the phase change from supercritical to high pressure ices (VII or X) is neglected because the temperature/pressure region remains widely unknown in this region.

Figure 2 represents the mass/radius relationships of supercritical ocean planets calculated in the 0.6–20 $M_\oplus$ range for equilibrium temperatures of 300, 650, and 1200 K, corresponding to distances of 0.72, 0.15, and 0.04 au from a solar-type star, respectively, assuming an Earth-like albedo. We explore different interior compositions, ranging between the two extreme and unrealistic cases of pure core and pure supercritical water (SW) compositions, to compare the effects on the resulting observables. The presence of a thick H_2O-dominated atmosphere generates a strong runaway greenhouse effect causing the presence of a supercritical hydrosphere, even if the equilibrium temperature of the planet is lower than the critical temperature of water ($T_{\mathrm{critical}} \sim 650$ K). Because the core–mantle boundary is not firmly defined at very high pressure and temperature (Hakim et al. 2018), we assume here the core and mantle form a unique phase constituted of silicate rocks, including bridgmanite $(Mg,Fe)SiO_3$ and ferro-periclase (Mg,Fe)O (Brugger et al. 2017).

Figure 2 shows that some members of the sub-Neptunes population can be well matched by mass/radius curves corresponding to ocean planets with significant supercritical hydrospheres. For the sake of comparison, the sub-Neptune K2-38b, in which H_2O absorption bands have been recently observed (Benneke et al. 2019b), is also represented in Figure 2. If one considers the central values of its measured mass and radius ($M_p = 8.63\ M_\oplus$ and $R_p = 2.61\ R_\oplus$; Benneke et al. 2019b), the composition of this planet cannot be explained via the use of classical super-Earths interior models, and requires an extra amount of hydrogen–helium. On the other hand, it is fully matched by models made by a rocky core–mantle topped by a supercritical water layer and a steam atmosphere irradiated at 300 K, a value close to the equilibrium temperature estimated to be ∼257 K (Benneke et al. 2019b). In this case, the mass fraction of incorporated water is ∼37%, a value in the same range as those derived for the water worlds in our solar system.

4. Discussion

Our model explores the assumption of water-rich and supercritical planets as an alternative or a complement to sub-Neptunes with hydrogen/helium gaseous envelopes. This indeed does not exclude the existence of such mini-giants but suggests that super-Earths and a fraction of sub-Neptunes could belong to the same family of planets, with differences between their interiors simply resulting from the variation in the water content.

[6] http://www.iapws.org/relguide/MeltSub.html

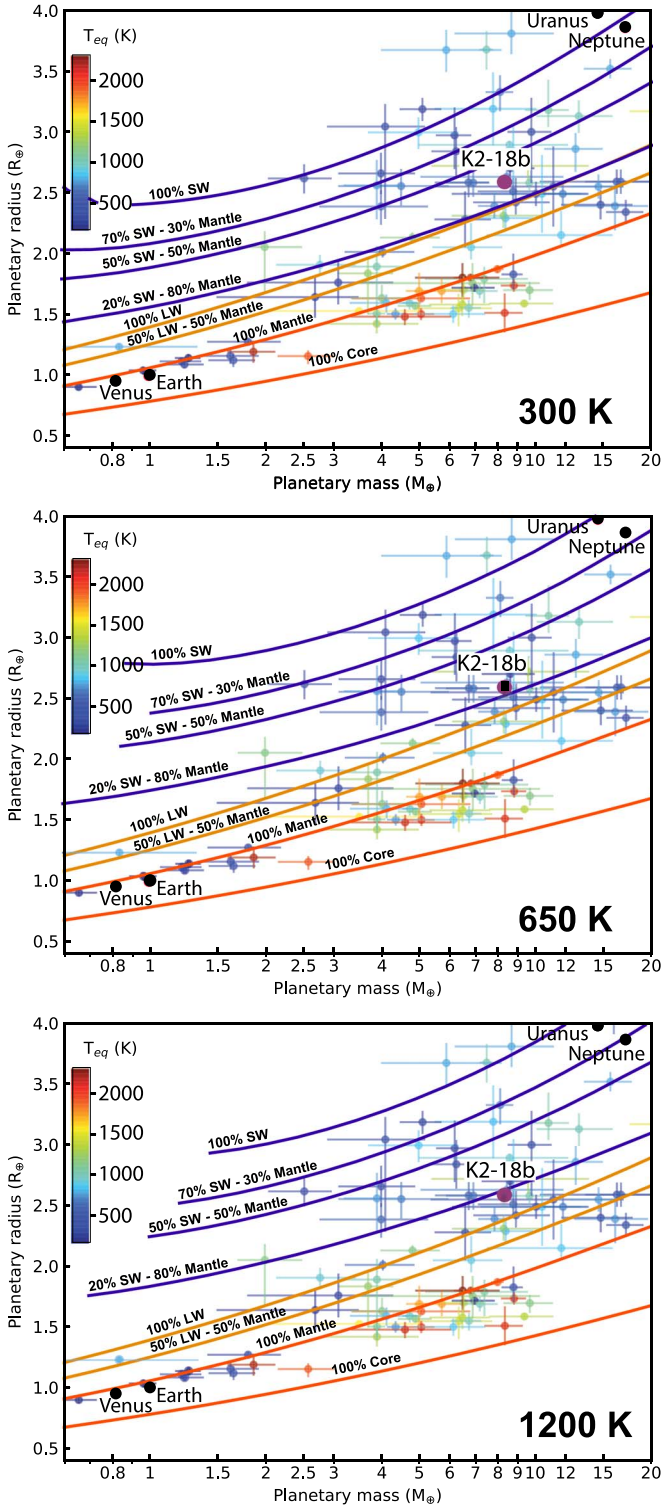

Figure 2. Mass–radius diagrams determined for exoplanets with masses in the 0.6–20 $M_\oplus$ range, and equilibrium temperatures of 300, 650, and 1200 K. Mass–radius curves are calculated for several planetary compositions: 100% core and 100% mantle (red curves), liquid water (LW) hydrosphere (brown curves), and supercritical water (SW) hydrosphere (blue curves) topping mantle-like composition interiors. Planetary data are taken from the NASA exoplanet archive and updated to 2019 July 20. Hydrostatically unstable atmospheres (defined when the altitude at 0.1 Pa tends toward infinity) around the hotter and smaller planets are excluded from the mass–radius relationships.

Because of the proximity to their host star, for those that are water-rich, the strong insolation associated with a runaway greenhouse effect in their atmospheres generates inflated supercritical hydrospheres. As a result, they would exhibit larger radii compared to similar bodies with a very low water content located at higher distances to the star. Both Zeng & Sasselov (2014) and Thomas & Madhusudhan (2016) also found that small planets with supercritical water layers could exhibit larger radii than planets of the same masses with solid or liquid hydrospheres. However, these increases were found more moderate than those derived from our model because of the absence of coupling with water-rich atmosphere models. The same effect has been recently reported in the case of irradiated super-Earths displaying water steam atmospheres in contact with rocky mantles (Turbet et al. 2020). However, the outcomes of this study require a new assessment via the implementation of a dedicated supercritical water EOS in the atmosphere model. Meanwhile, our model also presents some limitations. The convergence observed in Figure 1 at the 1000 bar interface between the pressure–temperature profiles of the 15 $M_\oplus$ planet at 1200 K and the 1 $M_\oplus$ planet at 650 K corresponds to the use of an EOS for supercritical water in the atmosphere model different from the one employed in the interior model, and which slightly departs from its validity range.

We underline that high pressure ices such as Ice X and Ice XI (Zeng & Sasselov 2014) are not taken into account in our model. However, the pressure reached at the base of the hydrosphere of 20 $M_\oplus$ planets including 50% water is about 600 GPa with temperatures always greater than 4000 K. This temperature–pressure range, close to the one reached at the center of the 15 $M_\oplus$ pure water planet (500 GPa) shown in Figure 1, is out of the stability domain of Ice X and Ice XI (see Figure 1 of Zeng & Sasselov 2014). We therefore estimate that this effect should be marginal up to 20 $M_\oplus$. Also, high temperatures achieved at the base of the hydrosphere may be sufficient to induce melting of the silicate layer. As a result, much of the volatile content of the planet may actually be dissolved within the liquid silicate mantle (Kite et al. 2019, 2020).

Interestingly, planets possessing exactly the mass and radius of Neptune could be matched by ocean planets if the latter contain ~70% supercritical water, depending on their orbital distance and the type of their host star. Our model implies that both super-Earths and water-rich sub-Neptunes have grown from building blocks with a wide range of ice-to-rock ratios. This hypothesis is supported by recent dynamical simulations showing that the observed distributions of close-in small planets are matched by the presence of both ice-rich and dry planets (Izidoro et al. 2017, 2019). Water-rich small planets should have grown from ice-rich building embryos formed beyond the snowline in protoplanetary disks, while dry ones would have grown from rocky embryos formed within the snowline. Ice-rich embryos would have subsequently migrated inward the disk, catalyzing the growth of purely rocky planets interior to the ice-rich ones (Raymond et al. 2018a, 2018b).

Observations have shown that the population of small planets follows a bimodal distribution peaking at ~1.3 $R_\oplus$ (super-Earths) and 2.4 $R_\oplus$ (sub-Neptunes), with few planets in between (Fulton et al. 2017; Fulton & Petigura 2018). A study, combining planetary interior models based on a mixture of rocks and ices associated with Monte Carlo simulations, has

recently addressed this question (Zeng et al. 2019). The authors found that the 2–4 $R_\oplus$ planets should contain significant amounts of H_2O-dominated ices in addition to rock, with perhaps more than half, by mass. They also derived that planets with radii $>3R_\oplus$ would generally require the presence of a gaseous envelope. The physical assumptions formulated in this study are however questionable since highly irradiated water-rich close-in planets should display supercritical and inflated hydrospheres instead of being simply ice-rich. It has also been proposed that the gap between the super-Earths and sub-Neptunes could be accounted for by the evaporation of gaseous envelopes, due to the host star irradiation (Jin & Mordasini 2018; Owen & Murray-Clay 2018). The same process could also happen to water-rich sub-Neptunes displaying supercritical envelopes: studies of water loss from terrestrial planets orbiting ultracool dwarfs assume that photolysis, i.e., the conversion of H_2O steam into H_2 gas, is not a limiting process in the escape mechanism (Bolmont et al. 2017). The same assumption would remain valid in the case of stars displaying stronger FUV fluxes.

In summary, models of water-rich planets with supercritical envelopes can explain the observed physical properties of some of the planets among the small planet population. They offer an interesting alternative to the current dichotomy between rocky and gas-rich planets. This quantitative exploration of the role of supercritical water in planetary envelopes, which underlines the importance of composition in the case of strong irradiation, will be extended by the development of a model describing the planets' interior and atmosphere in a more consistent way. This work also highlights the need for improved EOSs in the high pressure and high temperature regime of the water phase diagram.

O.M. and M.D. acknowledge support from CNES. We acknowledge an anonymous referee whose comments helped improve and clarify this manuscript.

ORCID iDs

Artyom Aguichine https://orcid.org/0000-0002-8949-5956
Emmanuel Marcq https://orcid.org/0000-0002-1924-641X
Bastien Brugger https://orcid.org/0000-0002-6692-0753

References

Benneke, B., Knutson, H. A., Lothringer, J., et al. 2019a, NatAs, 3, 813
Benneke, B., Wong, I., Piaulet, C., et al. 2019b, ApJL, 887, L14
Bolmont, E., Selsis, F., Owen, J. E., et al. 2017, MNRAS, 464, 3728
Brugger, B., Mousis, O., Deleuil, M., et al. 2017, ApJ, 850, 93
Dorn, C., Venturini, J., Khan, A., et al. 2017, A&A, 597, A37
Duan, Z., Møller, N., & Weare, J. H. 1996, GeCoA, 60, 1209
Duan, Z., & Zhang, Z. 2006, GeCoA, 70, 2311
Frank, M. R., Fei, Y., & Hu, J. 2004, GeCoA, 68, 2781
Fulton, B. J., & Petigura, E. A. 2018, AJ, 156, 264
Fulton, B. J., Petigura, E. A., Howard, A. W., et al. 2017, AJ, 154, 109
Grimm, S. L., Demory, B.-O., Gillon, M., et al. 2018, A&A, 613, A68
Haar, L., Gallagher, J., Kell, G. & National Standard Reference Data System (U.S.) 1984, NBS/NRC Steam Tables: Thermodynamic and Transport Properties and Computer Programs for Vapor and Liquid States of Water in SI Units (Washington, DC: Hemisphere)
Hakim, K., Rivoldini, A., Van Hoolst, T., et al. 2018, Icar, 313, 61
Izidoro, A., Bitsch, B., Raymond, S. N., et al. 2019, arXiv:1902.08772
Izidoro, A., Ogihara, M., Raymond, S. N., et al. 2017, MNRAS, 470, 1750
Jin, S., & Mordasini, C. 2018, ApJ, 853, 163
Kasting, J. F. 1988, Icar, 74, 472
Kite, E. S., Fegley, B., Schaefer, L., et al. 2019, ApJL, 887, L33
Kite, E. S., Fegley, B., Schaefer, L., et al. 2020, ApJ, 891, 111
Léger, A., Selsis, F., Sotin, C., et al. 2004, Icar, 169, 499
Lopez, E. D., Fortney, J. J., & Miller, N. 2012, ApJ, 761, 59
MacDonald, R. J., & Madhusudhan, N. 2019, MNRAS, 486, 1292
Marcq, E. 2012, JGRE, 117, E01001
Marcq, E., Salvador, A., Massol, H., et al. 2017, JGRE, 122, 1539
Mousis, O., Atkinson, D. H., Cavalié, T., et al. 2018, P&SS, 155, 12
Ogihara, M., Morbidelli, A., & Guillot, T. 2015, A&A, 578, A36
Owen, J. E., & Murray-Clay, R. 2018, MNRAS, 480, 2206
Raymond, S. N., Boulet, T., Izidoro, A., et al. 2018a, MNRAS, 479, L81
Raymond, S. N., Izidoro, A., & Morbidelli, A. 2018b, arXiv:1812.01033
Rogers, L. A. 2015, ApJ, 801, 41
Thomas, S. W., & Madhusudhan, N. 2016, MNRAS, 458, 1330
Turbet, M., Bolmont, E., Ehrenreich, D., et al. 2020, A&A, 638, A41
Venturini, J., & Helled, R. 2017, ApJ, 848, 95
Wagner, W., & Pruß, A. 2002, JPCRD, 31, 387
Weiss, L. M., & Marcy, G. W. 2014, ApJL, 783, L6
Zeng, L., Jacobsen, S. B., Sasselov, D. D., et al. 2019, PNAS, 116, 9723
Zeng, L., & Sasselov, D. 2014, ApJ, 784, 96